

ATLAS Overview - Sub-detector Performance, Data Taking 2010, Highlights of Latest Results

Daniel Dobos* on behalf of the ATLAS Collaboration

TU Dortmund & CERN

E-mail: Daniel.Dobos@cern.ch

The performance of the detectors, the data taking in 2010 and the latest results of the ATLAS Experiment at CERN are presented.

Workshop on Discovery Physics at the LHC -Kruger 2010

December 05-10, 2010

Kruger National Park, Mpumalanga, South Africa

*Speaker.

2.7 with gas-based muon chambers in a air-core toroid magnet with 2-6 Tm for $|\eta| < 1.3$ and 4-8 Tm for $1.6 < |\eta| < 2.7$. It provides muon triggers and momentum measurement with a resolution 10% up to $E_\mu \approx 1$ TeV. Monitored Drift Tubes (MDT) and Cathode Strip Chambers (CSC) are used as precision detectors, Resistive Plate Chambers (RPC) and Thin Gap Chambers (TGC) are used as trigger detectors. A 3-stage trigger system reduces the 40 MHz bunch crossing frequency to a level-1 trigger frequency of 75 kHz and finally to a recording frequency between 200-300 MHz.

2. Inner Detector Performance

The hit association efficiency of a track crossing a pixel layer is shown for the different layers in Figure 2 in the top right plot. For all but the most external disks the efficiencies are about 99% and full efficiency of the B-Layer is caused by the track selection criteria. Lower efficiencies for the outermost disk are due to inefficient regions in some modules (dead modules are excluded from calculation, dead regions are not excluded). The bottom right plot shows the distribution of the real data local x (most precise pixel direction) unbiased residuals with the autumn 2010 alignment in close agreement (resolution: $19 \mu\text{m} \leftrightarrow 17 \mu\text{m}$) with the Monte-Carlo (MC) residuals of a perfectly aligned detector. The correlation of the Time-over-Threshold (ToT), which is proportional to the deposited charge, in units of bunch crossings with the hit cluster width in η direction is plotted for $\sqrt{s} = 7$ TeV for colliding and non-colliding bunches in the two lower, left plots. For colliding bunches an additional band with high ToT values but small cluster widths can be observed, being consistent with particles from the interaction point traversing the pixel planes with higher perpendicular components. In the top left plot the energy loss in pixels is shown, which allows low momentum distinction between the Bethe-Bloch rises of pions, kaons, protons and deuterons.

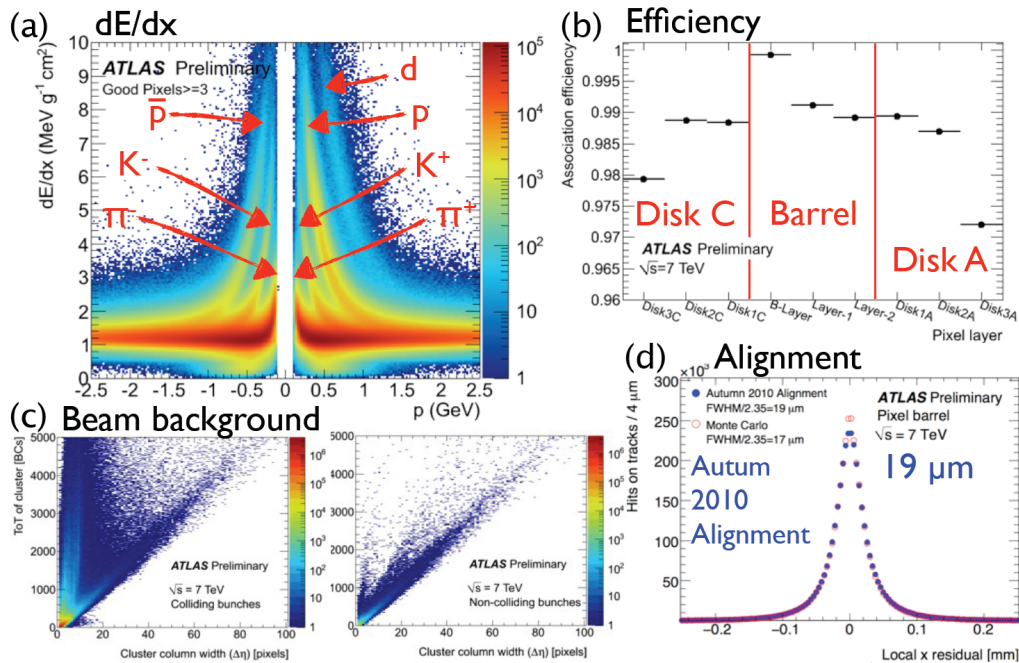


Figure 2: Energy loss (a), efficiency (b), beam background (c) and alignment (d) of the pixel detector.

In Figure 3 top left table the amount of disabled modules, readout chips and strips are listed for the endcap and the barrel SCT, altogether resulting in a disabled fraction of 0.97%. The top right plot shows the intrinsic module efficiency for ID combined and SCT-only tracks for different barrel layers. With dead modules and chips taken into account the overall hit efficiency is $99.8 \pm 0.1\%$ (see yellow band). The bottom right shows the distribution of the real data local x (across the microstrip direction) unbiased residuals with autumn 2010 alignment in close agreement (resolution: $36 \mu\text{m} \leftrightarrow 34 \mu\text{m}$) with the MC residuals of a perfect alignment. The measurement of the average hit cluster size versus the incident angle is show in the bottom right plot for cosmic data and MC with and without magnetic field. The minimum of the 'no B-field' data is consistent with a zero incident angle and the minimum of the 'with B-field' data is used to extract the Lorentz angle. The top left plot of Figure 4 shows the probability of a TRT high-threshold (HT) hit as function of

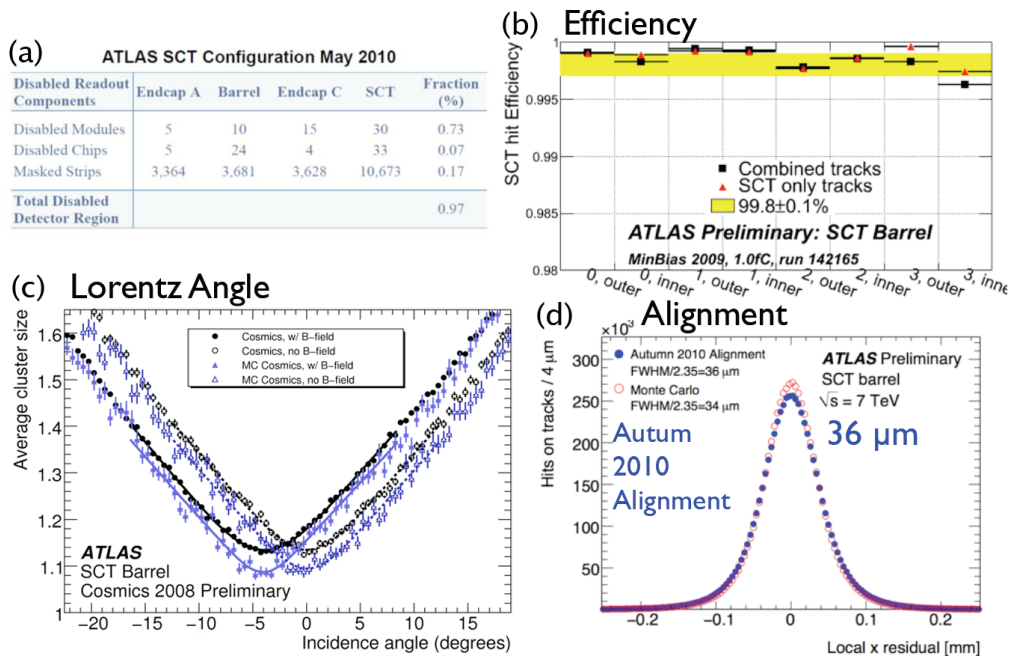


Figure 3: Efficiency (a) & (b), Lorentz angle (c) and alignment (d) of the SCT detector.

the Lorentz γ -factor for TRT barrel measured with 900 GeV collisions and simulated with MC. For particles with a γ -factor above 1000 the probability for a HT hit increases due to the production of transition radiation. This enables the TRT to separate pions and electrons between 1 GeV and 150 GeV momentum. The ToT distribution for pions and electron candidates obtained from 7 TeV collision data is shown on the top left and demonstrates the capability to use it as an additional separating variable for particle identification. The distribution of the residuals in the bottom left plot shows an excellent agreement between the autumn 2010 alignment with the MC residuals of a perfectly aligned detector with a resolution of $34 \mu\text{m}$. In the bottom right plot the specific energy loss based on the TRT measured ToT is shown and demonstrates that this variable can be used for particle identification for heavily ionizing particles by showing the typical Bethe-Bloch rises for protons and kaons. Also deuterons can be seen with a $|d_0| > 1 \text{ mm}$ selection.

The performance of the combined inner detector tracking system can be see in Figure 5. Res-

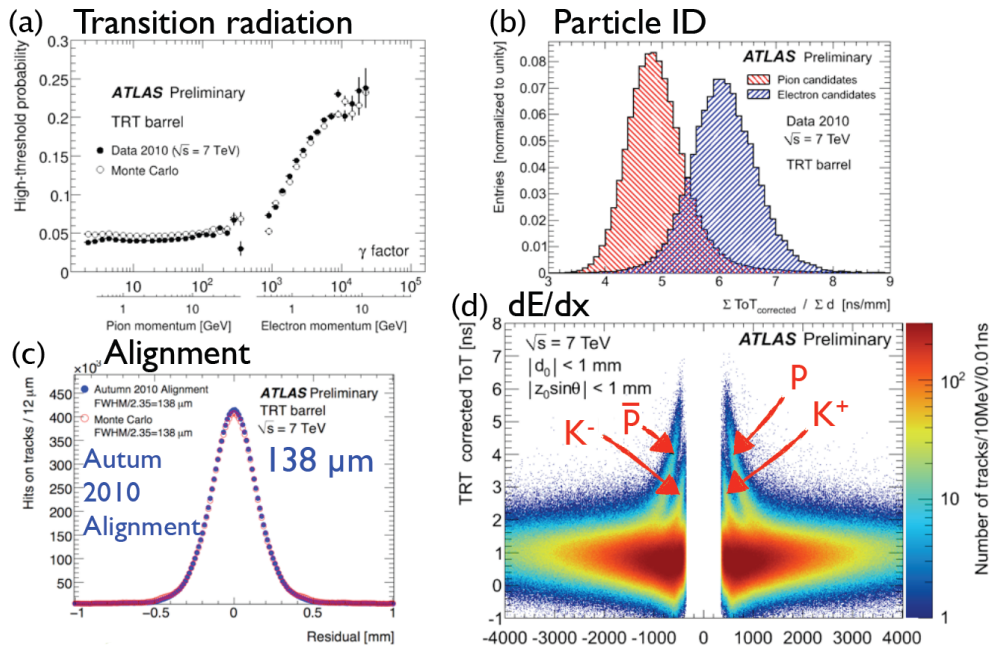


Figure 4: TRT detector alignment (c) and its particle identification using transition radiation (a), ToT (b) and dE/dx (d).

onances, for example J/ψ , are used to study the mass resolution and accuracy of momentum with ID tracks. The top row plots show the $m_{J/\psi}$ peak, its comparison with MC simulation and the PDG [3] value as well as the mass resolution for four pseudorapidity bins. In the lower row is shown the two-dimensional distribution of the primary vertex with a slightly tilted interaction point in x direction as well as the primary vertex resolution dependency on the transverse momentum sum.

3. Calorimeter Performance

Performance plots of the electromagnetic LAr calorimeter are shown in Figure 6. On the top left the barrel cell energy distribution for $\sqrt{s} = 900$ GeV collision candidates as well as the cell energy distribution of random data (electric noise only) and of non-diffractive minimum bias MC events are shown. The η versus ϕ cell occupancy map for 7 TeV collision data is shown on the top right. About 1.3% of the LAr calorimeter have dead readout and 6% have an increased noise due to cell energy corrections necessary for non-nominal HV regions. Very high occupancy is visible for 0.1% of problematic cells. The Forward Calorimeter (FCal) energy density map is shown in the bottom left plot. It measures the relative position of the FCal to the beam spot by analyzing the ϕ distribution. The timing of the LAr barrel, i.e. the average time per front end board, is shown in the bottom middle and reaches an RMS of 1 ns level.

The top left plot in Figure 7 shows the TileCal cell energy distribution for 0.9, 2.36 and 7 TeV collision data in comparison to 7 TeV minimum bias MC events and random trigger events. The average Transverse Energy Sum ΣE_T of collision candidates and non-diffractive minimum bias MC events as function of η is shown on the top right. With a TileCal cells $E_T > 500$ MeV selection

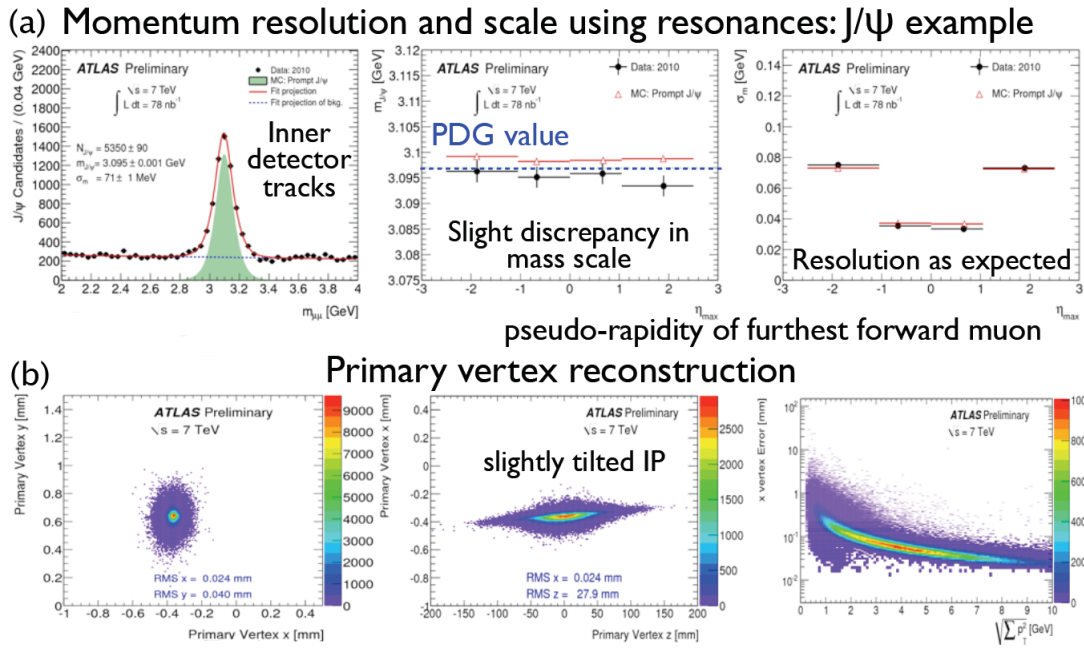


Figure 5: Inner detector J/ψ mass peak, mass scale, mass resolution (a) and primary vertex resolution (b).

for both distributions, in order to have negligible electronics noise contribution, they show good agreement. The average time over all cells with the same ϕ coordinate (azimuth) as a function of the cell z coordinate (beam axis direction) is shown for single beam data (Beam 1) in the bottom left plot. The three radial sampling layers are represented by different colors. The measured slope corresponds to the muon time of flight along the z direction to cross the TileCal and results with time of flight correction in a resolution of 0.45 ns RMS shown in the bottom right plot.

Figure 8 shows the combined calorimeter performance. The top row plots show E/p versus track momentum data of 7 TeV collisions and the corresponding non-diffractive minimum bias MC for the barrel $0.0 < |\eta| < 0.6$ and the forward $1.9 < |\eta| < 2.3$ pseudorapidity regions. The data to MC agreement is within 5% in both regions. The selection efficiency relative to track jets versus track jet transverse p_T plots for 7 TeV collisions in data and MC demonstrates full efficiency for $p_T > 15$ GeV. The ratio of the relative efficiency between data and MC show as well a 5% agreement over the entire track jet p_T range.

4. Muon Spectrometer Performance

Figure 9 top left shows the MDT segment residuals with 7 TeV data and its fit with a double Gaussian function resulting in an intrinsic resolution of $91.6 \mu\text{m}$. In the top right the MDT chambers space time relationship, showing the relation between drift distance and drift time, is shown. The accurate timing (with a RMS of 11.79 ns) of the MDT chambers can be quantified by comparing the T_0 s (the drift tube timing offsets) obtained with Beam 1 and Beam 2 splash events in the bottom left. The distribution of the number of MDT hits on combined muon tracks is shown in data and MC predictions for 7 TeV collisions in the bottom right plot.

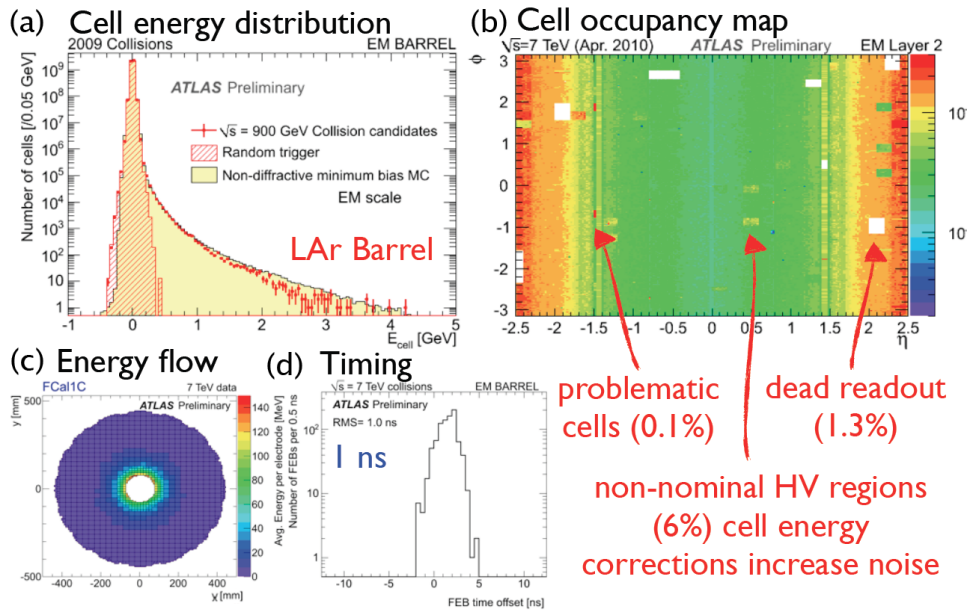


Figure 6: LAr cell energy distribution (a), occupancy map (b) and timing (d); FCal energy flow (c).

The Muon Spectrometer sagitta resolution for large and small barrel sectors as a function of muon momentum can be seen in Figure 10 top left. Dedicated commissioning runs with toroid field off were taken, where the track momenta were measured with the ID. Based on this data the muon spectrometer sagitta resolution was determined to be $80 \mu\text{m}$ and $101 \mu\text{m}$ for the large and small sectors. The transverse momentum resolution as a function of p_T with an empirical fit including a quadratic sum of an energy loss fluctuation term p_0/p_T , a multiple scattering term p_1 and a spectrometer resolution term $p_2 \times p_T$ is shown in the bottom left. The $\Delta p/p$ distribution for combined muons to validate the prompt muon component with J/ψ is shown on the top right. The best fit, a fit of the prompt and the pion / kaon component are shown as well. In the bottom right plot the muon reconstruction efficiency as function of the transverse momentum are shown for muon spectrometer stand-alone reconstruction, combined muon spectrometer track with ID track reconstruction and for the combination of these with segment tags (ID track and a muon spectrometer straight-line segment).

5. Data Taking Operation 2010

Figure 11 shows the integrated delivered proton-proton luminosity versus time at ATLAS and the corresponding integrated recorded luminosity. Event views of the 2010 proton-proton operation milestones are showing the first W, Z and top quark candidate as well as a dijet event at a mass of 3.1 TeV. The total integrated luminosity of the delivered collisions is 48 pb^{-1} , out of which 45 pb^{-1} could be recorded, which results in an overall luminosity weighted data taking efficiency of 94%. The luminosity detectors were calibrated with Van der Meer scans to a level of 11%, with a 5% calibration reachable in the near future. The instantaneous peak luminosity reached $2.07 \times 10^{32} \text{ cm}^{-2}\text{s}^{-1}$.

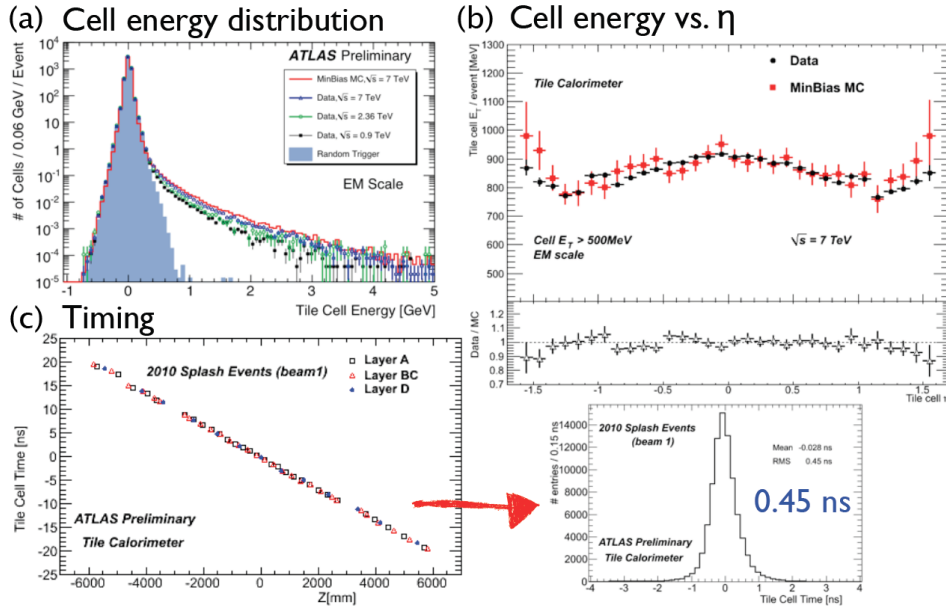


Figure 7: Cell energy distribution (a), cell energy versus η (b) and timing (c) of the tile calorimeter.

Of the total 88 million ATLAS data channels, the fraction of good channels is $> 97\%$ for all subsystems. The good marked data fraction, determined from detailed quality checks and noise and dead channel maps from 36-hour calibration loops on 10% of the data, is above 99% for the inner tracking detectors, above 96.2% for muon detectors and between 90.5 and 97.8% for the calorimeters. A future data reprocessing will largely recover the calorimeter inefficiencies. The few percent losses in the silicon and muon detectors are due to safety procedure in case of non stable beam conditions for which the HV must be ramped down in the ID and the muon detectors.

For the worldwide data distribution and analysis ATLAS reached in 2010 total data throughputs in the Grid above the 2 GB/s design value several times. High occupancy throughput peaks of 10 GB/s have been reached during critical periods such as the start of the 7 TeV data taking, data and MC re-processing or during the heavy ion run.

With increasing luminosity pile-up events are becoming more important. For example at a luminosity $L \approx 1.6 \times 10^{30} \text{ cm}^{-2}\text{s}^{-1}$ in average 1.3 pp interactions occur, i.e. $\approx 40\%$ pile-up events. Collisions with four pile-up vertices separated by 51 mm have been observed. With 10-45 $p_T > 150 \text{ MeV}$ tracks per vertex still a good vertex resolution below $200 \mu\text{m}$ can be reached.

During the 2010 operation the 3-level trigger system (level-1, level-2 and Event Filter (EF), with level-2 & EF also called High Level Trigger (HLT)) were operated in $\approx 300 \text{ Hz}$ data record mode. For luminosities less than $10^{27} \text{ cm}^{-2}\text{s}^{-1}$ a trigger of Minimum Bias Trigger Scintillators (MBTS) located at $z = \pm 3.5 \text{ m}$ from the interaction point and the HLT running in transparent mode was used. Above $L = 10^{27} \text{ cm}^{-2}\text{s}^{-1}$ the MBTS triggers were prescaled, whereas electron, photon, jet, tau and muon triggers remained un-prescaled. At $L = 10^{29} \text{ cm}^{-2}\text{s}^{-1}$ HLT e/γ chains were activated to cope with the increasing rates while running with low level-1 trigger thresholds and prescaled lowest jet thresholds. HLT chains were activated at $L = 3.5 \times 10^{29} \text{ cm}^{-2}\text{s}^{-1}$ for the

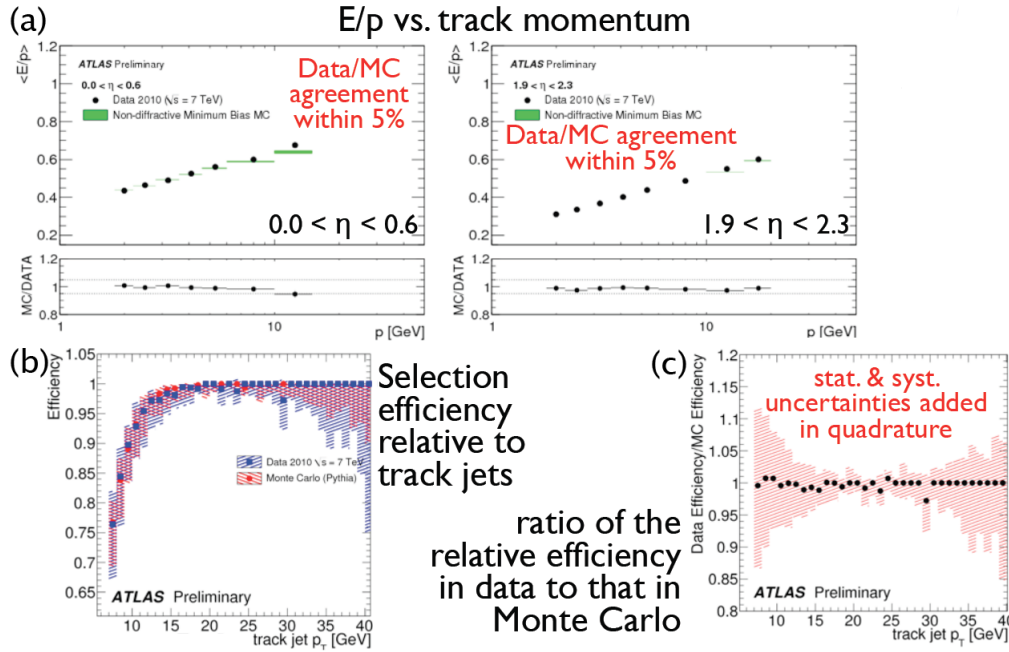


Figure 8: Combined calorimeter E/p (a) and jet selection efficiency relative to track jets (b) & (c).

lowest tau threshold, at $L = 6 \times 10^{29} \text{ cm}^{-2} \text{ s}^{-1}$ for the lowest forward muon threshold.

Examples of trigger performance plots are shown in Figure 12. The level-1 lowest threshold jet trigger efficiency, crucial for the jet cross section measurement is shown on the top left. Trigger efficiency for the lowest threshold level-1 forward muon trigger, important for di-muon resonances, is shown in the top right plot. The bottom left plots shows the level-1 tau trigger efficiency, important for SM and SUSY measurements. Important especially for $J/\psi \rightarrow ee$ measurements is the HLT tracking efficiency for electron candidates show on the bottom right.

The ATLAS maintenance plan for the LHC 2010 winter shutdown includes to open both detector sides to replace LAr optical data transmitters, which showed 29 failures so far affecting about 2% of the front end boards. A subset of the tile calorimeter power supplies are going to be replaced in parallel and preventive maintenance on the cryogenics, vacuum and safety systems are to be performed. Due to the complex opening and closing procedure only 2 out of the total 9 weeks of shutdown can be used for maintenance work.

6. Tracking and E_T^{miss} Performance

Important validations of the tracking performance are the mapping of the material with photon conversion and reconstruction of secondary vertices, as well as B-tagging efficiencies and soft QCD particle multiplicities and momentum spectra in pp minimum bias events. Other validations are performed by analyzing mass peaks, cascades and $J/\psi \rightarrow ee$. ATLAS observed all most classic resonances like K_S , K^* , ϕ , Λ , Ω , Ξ , D , D^* and J/ψ , for some of them the invariant mass distributions are shown in Figure 13. In this low mass regime the momentum scale is known to the permil and good agreement with the PDG values is observed.

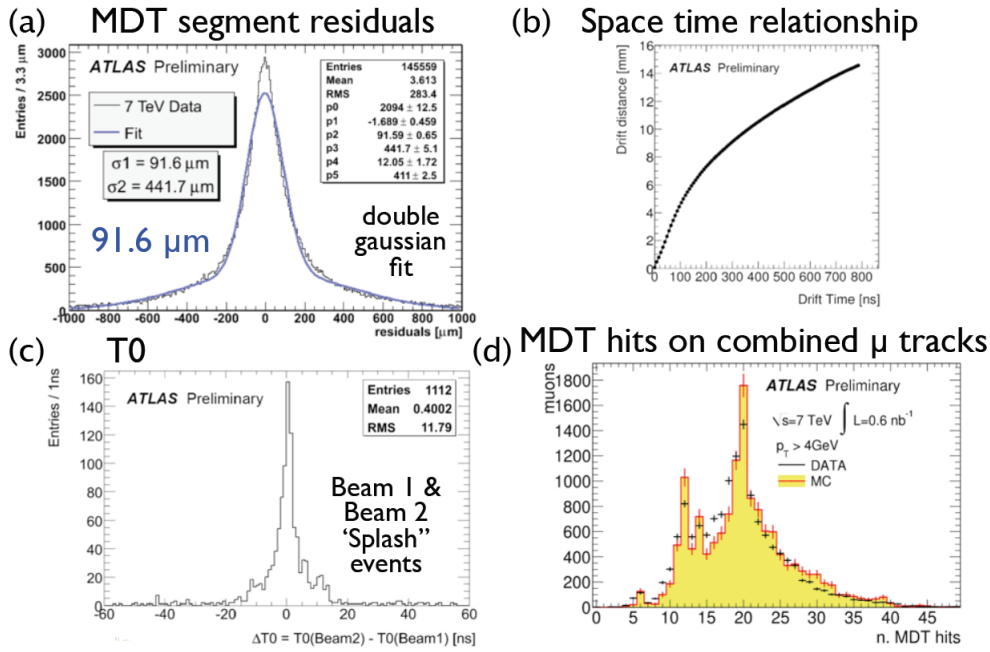


Figure 9: MDT segment residuals (a), space time relationship (b), timing (c) & hit number distribution (d).

The missing transverse energy E_T^{miss} is determined from the missing energies E_x^{miss} and E_y^{miss} , which are measured in about 200k cells over the full calorimeter coverage of 360° and $|\eta| < 4.5$. It is sensitive to the calorimeter hermiticity and resolution, cosmics and beam related backgrounds. Noise, coherent noise, dead cells, mis-calibrations and cracks are degrading the performance of the E_T^{miss} measurement. The E_x^{miss} , E_y^{miss} resolution versus ΣE_T for minimum bias events in comparison to MC simulated events and in comparison to a data subsample with $p_T > 20 \text{ GeV}$ jet events show good agreement in Figure 14. In ATLAS the uncertainty of the jet energy scale reached around 7% and improvements towards the 1% goal are expected.

7. J/ψ , W, Z and Top Quark

Figure 15 shows the di-muon and di-electron spectra in 7 TeV collisions. The di-muon selection is based on a leading muon with $p_T > 15 \text{ GeV}$ and a second leading muon with $p_T > 2.5 \text{ GeV}$. For the di-electron selection a 5 GeV E_T di-electron trigger is used, where the trigger selection produces a shoulder around 15 GeV. The J/ψ is one of the first 'standard candles' for detector commissioning and early physics, like B-physics or QCD, as it provides a large sample of low- p_T muons. It allows for the study of the muon trigger and identification efficiencies, momentum resolution (2% level) and absolute scale (0.2% level) in the few GeV range. For $J/\psi \rightarrow e^+e^-$ a mass resolution of $0.07 \pm 0.01 \text{ GeV}$ was reached with the first 78 nb^{-1} of data, for $J/\psi \rightarrow \mu^+\mu^-$ the resolution is $57 \pm 1 \text{ MeV}$ with the first 290 nb^{-1} .

Observation of the W and Z bosons are the fundamental milestones in the rediscovery of the Standard Model at 7 TeV and both of these bosons are powerful tools to constrain the q,g distributions inside the proton. The $Z \rightarrow ll$ process is used to calibrate the detectors to their ultimate

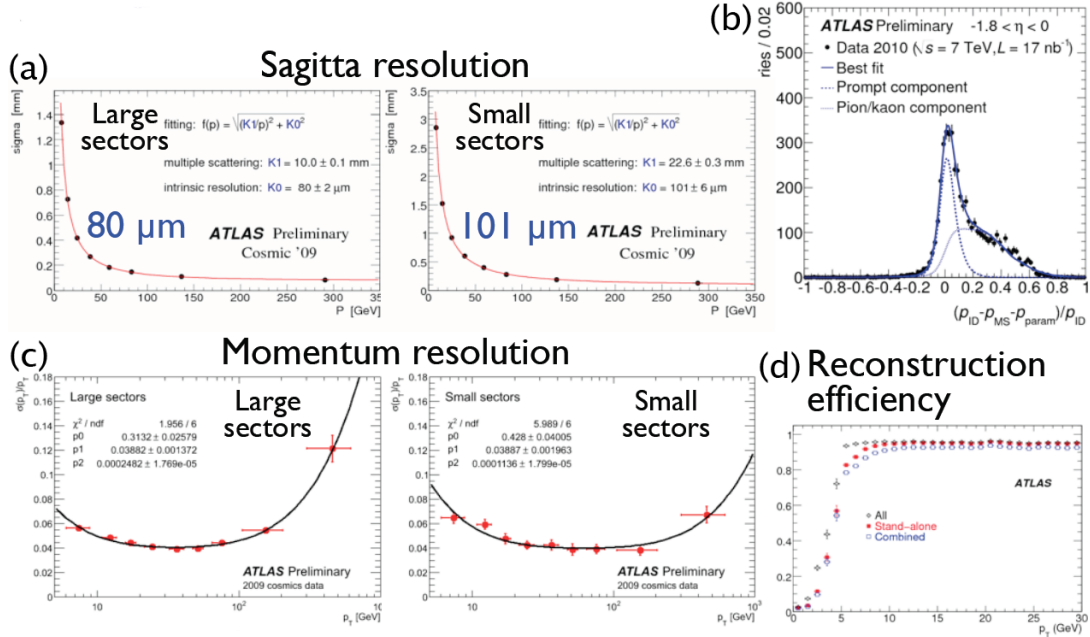
Validate prompt muon component with J/ψ 

Figure 10: Muon Spectrometer sagitta (a) and momentum resolution (c), reconstruction efficiency (d) and prompt muon component (b).

precision, as it allows for the study of the energy and momentum scales and resolutions in the EM calorimeter, tracker and muon spectrometer as well as the lepton identification efficiency. Figure 16 shows the invariant mass distributions for $Z \rightarrow ee$ in comparison to the MC and the improved data to MC agreement after the Autumn 2010 reprocessing for $Z \rightarrow \mu\mu$. E_T^{miss} distributions for $W \rightarrow e\nu$ and $W \rightarrow \mu\nu$ with an integrated luminosity of 3 pb^{-1} in comparison to their MC simulations with their signal and background components are shown in Figure 17. The cross-sections for W and Z were measured with an integrated luminosity of 300 nb^{-1} and show good agreement with PDG values.

An event view of a textbook example two lepton channel top candidate with two b-tagged jets with secondary vertices decay lengths of 3.9 mm and 4 mm and 4 GeV and 2 GeV secondary vertices vertex mass is shown in Figure 18. An electron with $p_T = 66 \text{ GeV}$ and a muon with $p_T = 51 \text{ GeV}$ were found. Jet multiplicity distributions (for $e + \text{jets}$ and $\mu + \text{jets}$) for pre-tagged and b-tagged top quark candidates were presented for an integrated luminosity of 2.9 pb^{-1} in good agreement with MC simulation. Jets are b-tagged for this analysis by a secondary vertex algorithm. The estimate of the QCD background is data-driven. Single top and $W/Z + \text{jets}$ background are determined from MC@NLO [4] and ALPGEN [5] Monte Carlo.

8. Heavy ion Collisions

In 2010 ATLAS recorded $8.25 \mu\text{b}^{-1}$ of the $8.67 \mu\text{b}^{-1}$ 2.76 TeV heavy ion collisions delivered by the LHC. The total integrated luminosity versus time is shown in Figure 19 bottom left. Events

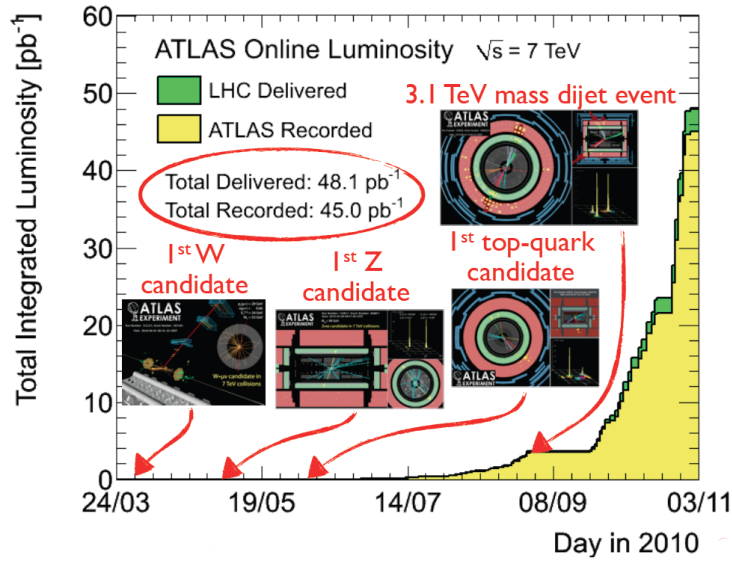


Figure 11: Integrated luminosity of 2010 LHC delivered 7 TeV collisions and ATLAS recorded events.

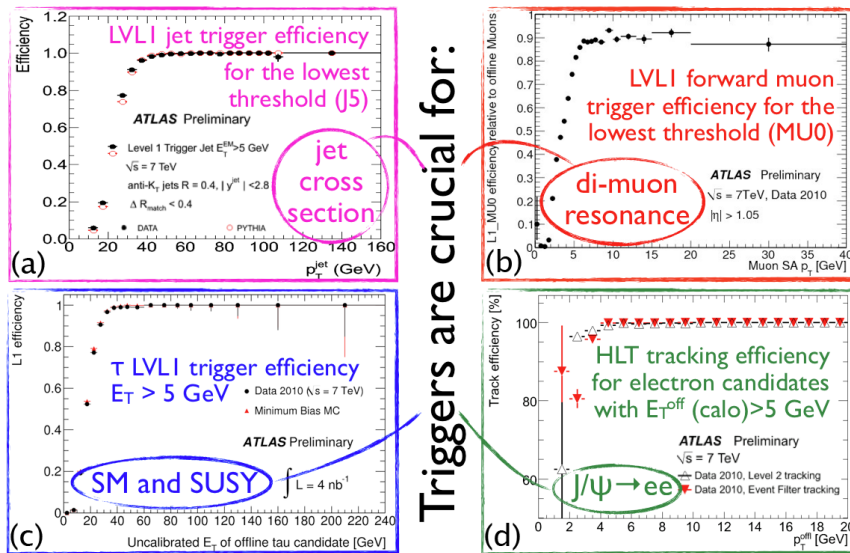


Figure 12: Examples of trigger efficiencies: lowest jet (a) and μ thresholds (b), τ trigger (c) and HLT electron tracking (d).

with an asymmetry between the transverse energies of the leading and the second jet have been observed [2]. An example event view of a highly asymmetric dijet event without evident recoiling jet and with high energy calorimeter cell distributed over a wide azimuthal region is shown in the top. In the bottom middle plot the event centrality is shown. It is characterized by using the total FCal transverse energy, according to fractions of the total lead-lead cross section and expressed in term of percentiles. A tight correlation between the near midrapidity energy flow and the forward ΣE_T (bottom right) verifies a clear correlation of the ΣE_T with the geometry of the overlap region

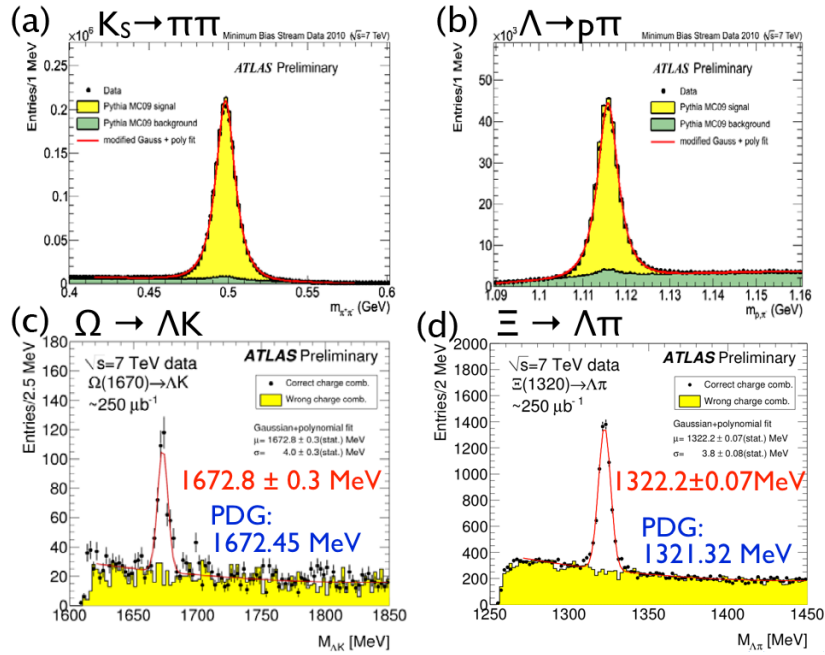


Figure 13: Validation of tracking performance with all most classic resonances.

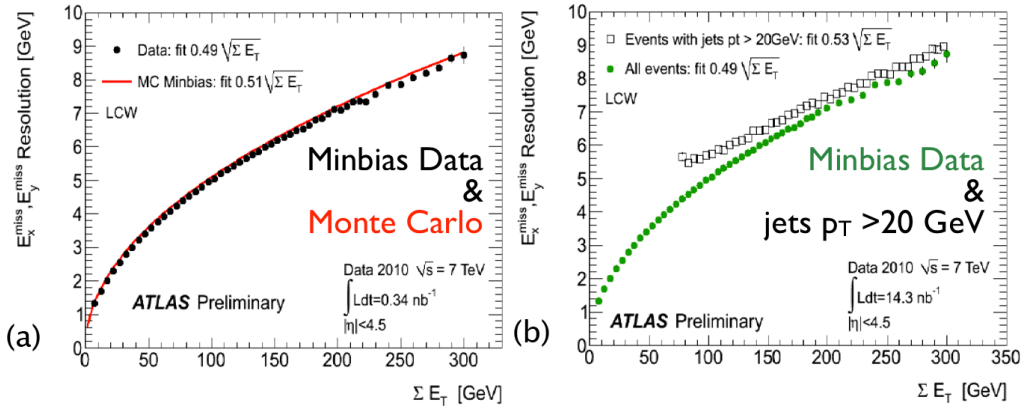


Figure 14: E_T^{miss} resolution versus ΣE_T for minimum bias data, MC (s) and $p_T > 20$ GeV jet events (b).

of the colliding nuclei. Figure 20 shows the dijet asymmetry and azimuthal angle between two jets distributions in four centrality bins. The lead-lead collision data is compared to proton-proton collision data and HIJING [6] + PYTHIA [7] simulated MC events. The observed asymmetry has a natural interpretation in terms of QCD energy loss, where the second jet is attenuated, in some cases leading to striking highly-asymmetric dijet events. This observation is the first of an enhancement of such large dijet asymmetries, not observed in proton-proton collisions, which may point to an interpretation in terms of strong jet energy loss in a hot, dense medium.

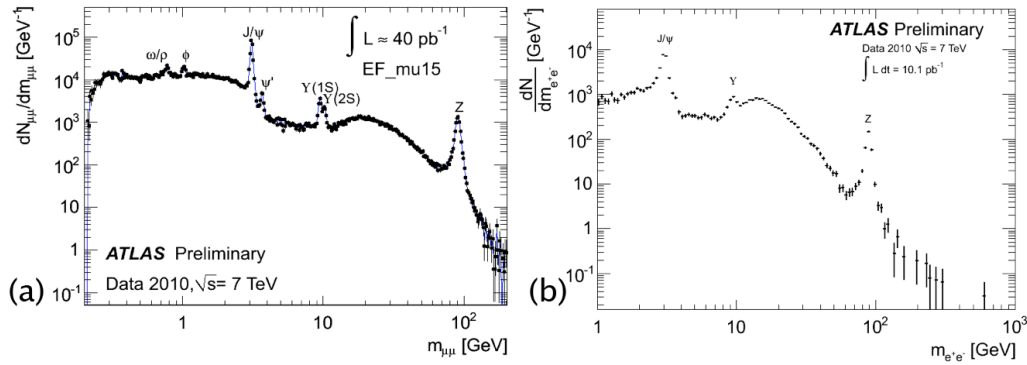


Figure 15: Dimuon (a) and dielectron (b) spectra of 7 TeV collisions.

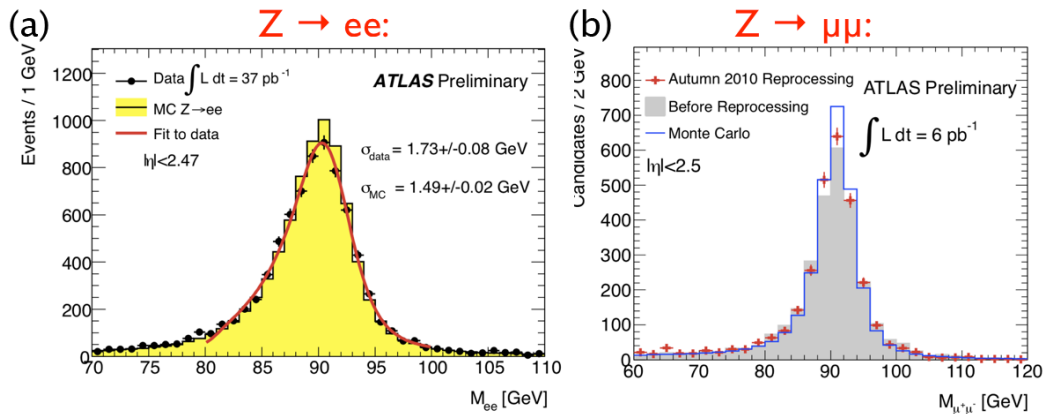


Figure 16: Dielectron (a) and dimuon (b) invariant mass in data, $Z \rightarrow ee$ and $Z \rightarrow \mu\mu$ Monte Carlo.

9. Conclusions

In 2010 ATLAS successfully collected 45 pb^{-1} proton-proton collision data during the first LHC run at $\sqrt{s} = 7 \text{ TeV}$. The entire experiment has worked efficiently and fast from data taking at the pit with an efficiency of 94%, data processing and transfer worldwide to the delivery of performance and physics results. First data demonstrates that the detector performance, like resolutions and efficiencies, and the quality of the reconstruction are better than expected. They are in agreement with detailed simulation. Years of test beam activities, increasingly realistic simulations and commissioning with cosmics were fundamental for such a good turn-on year. Production cross sections and properties of jets, W, Z, J/ψ have been measured, while top and tau candidates were observed. The search for new physics at the TeV scale has begun. The first heavy ion run successfully collected $8.25 \mu\text{b}^{-1}$ with a data taking efficiency of $> 95\%$. The observations and results are very encouraging. ATLAS is ready and has started to exploit the full physics potential of the LHC and a big, big thanks goes out to our LHC colleagues for this possibility.

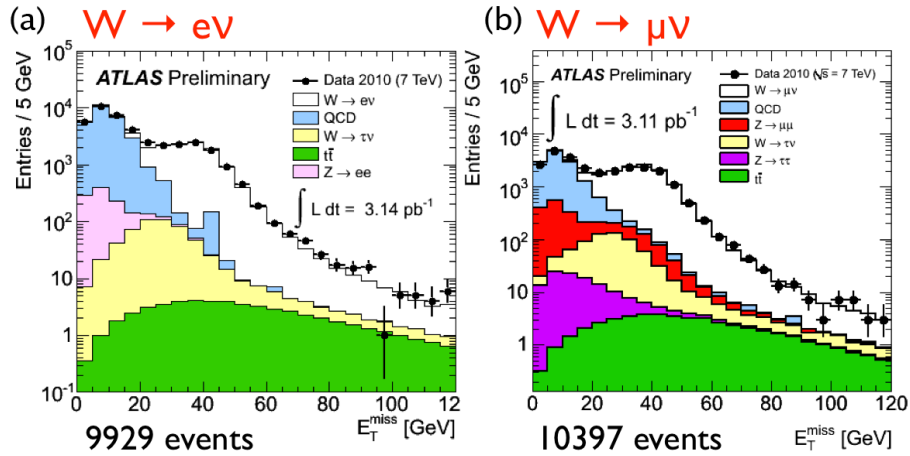


Figure 17: E_T^{miss} distributions for $W \rightarrow e\nu$ (a) and $W \rightarrow \mu\nu$ (b).

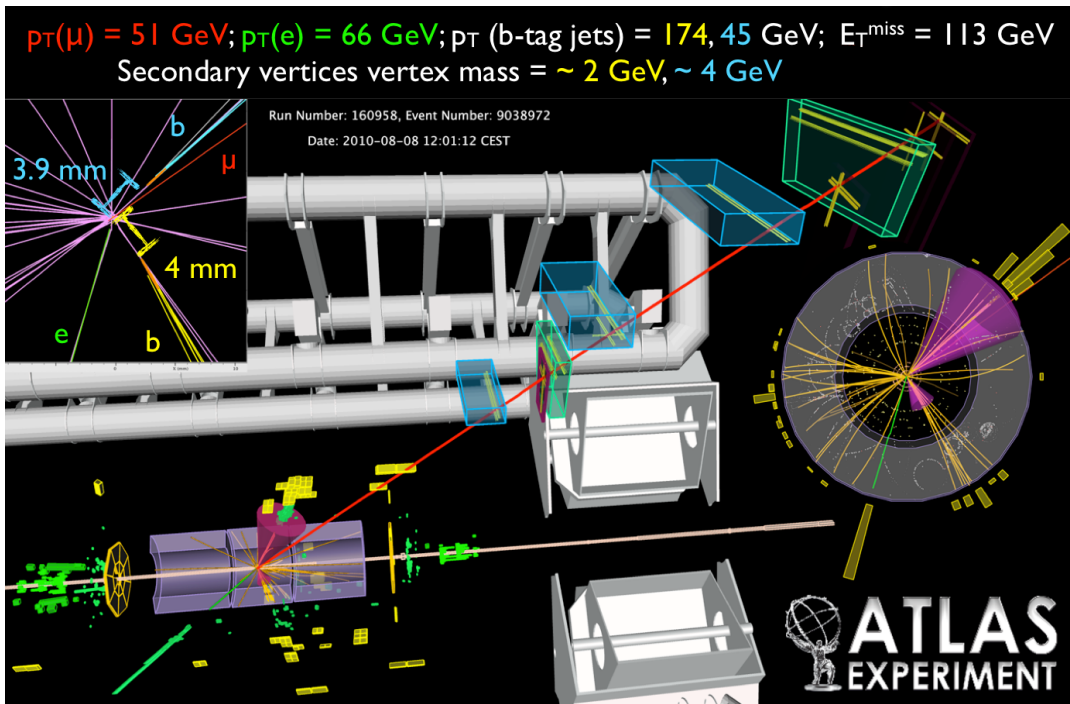


Figure 18: Event view of a textbook top candidate with two b-tagged jets, an electron and a muon.

References

- [1] The ATLAS Collaboration [G. Aad et al.], *The ATLAS Experiment at the CERN Large Hadron Collider*, JINST **3**:S08003,2008.
- [2] The ATLAS Collaboration [G. Aad et al.], *Observation of a Centrality-Dependent Dijet Asymmetry in Lead-Lead Collisions at $\sqrt{s} = 2.76$ TeV with the ATLAS Detector at the LHC*, Phys. Rev. Lett. **105**:252303,2010.

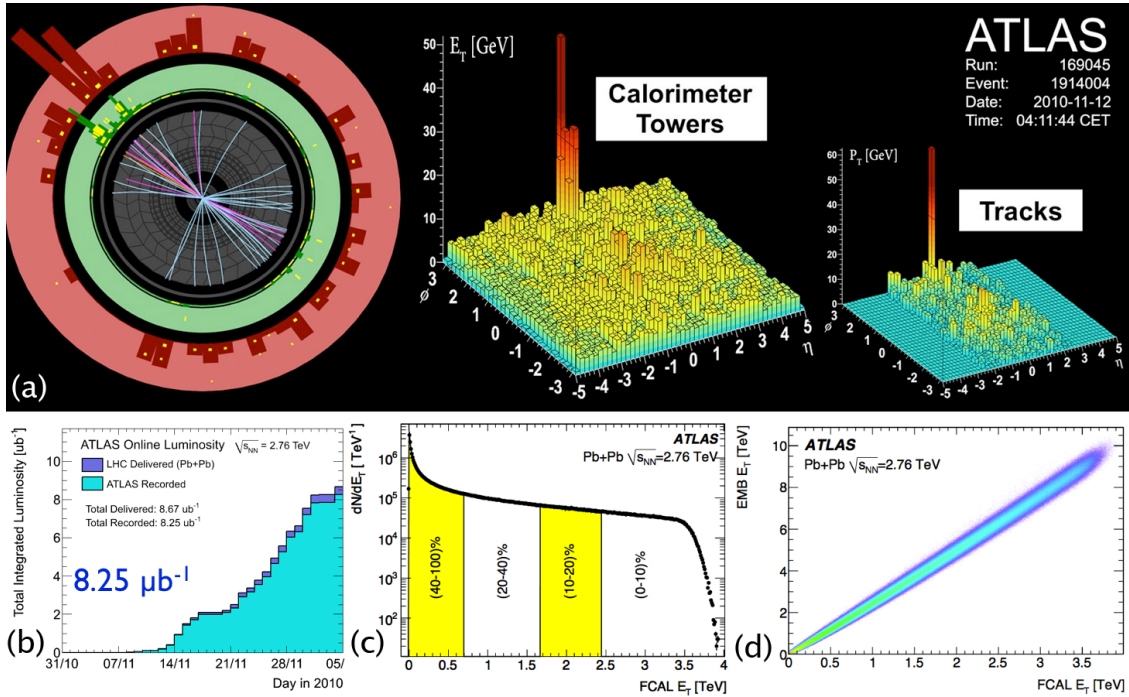


Figure 19: Centrality-Dependent dijet asymmetry in 2.76 TeV heavy ion lead-lead collisions.

- [3] Particle Data Group [K. Nakamura et al.], *Review of Particle Physics* J. Phys. G **37**, 075021 (2010).
- [4] S. Frixione, B. R. Webber, *Matching NLO QCD Computations and Parton Shower Simulations*, J. High Energy Phys. **06** (2002) 029.
- [5] M. L. Mangano, M. Moretti, F. Piccinini, R. Pittau, A. Polosa, *ALPGEN, a generator for hard multiparton processes in hadronic collisions*, J. High Energy Phys. **07** (2003) 001
- [6] Wang Xin Nian, M. Gyulassy, *HIJING : a Monte Carlo model for multiple jet production in pp, pA, and AA collisions*, Phys. Rev. D **44** (1991) 3501-3516.
- [7] H.-U. Bengtsson and T. Sjostrand, *The Lund Monte Carlo for hadronic processes - PYTHIA version 4.8*, Computer Physics Commun. **46** (1987) 43.

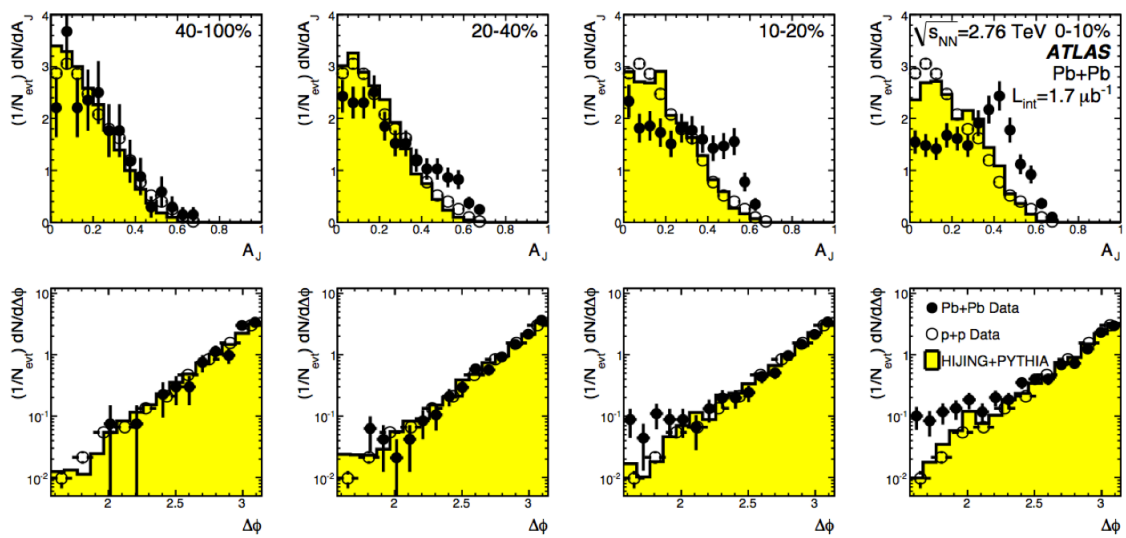


Figure 20: Dijet asymmetry and azimuthal angle between two jets distributions as a function of collision centrality.